Dynamics of an assembly of rigid ice floes

Matthias Rabatel, Stéphane Labbé, Jerome Weiss

HAL Id: hal-01907708

https://hal.science/hal-01907708

RESEARCH ARTICLE

Correspondence to:
M. Rabatel,
matthias.rabatel@imag.fr

Dynamics of an assembly of rigid ice floes

Matthias Rabatel[1], Stéphane Labbé[1], and Jérôme Weiss[2]

[1]Laboratory Jean Kuntzmann, Université Grenoble Alpes, Gières, France, [2]ISTerre, CNRS UMR 5275, Université Grenoble Alpes, Saint-Martin d'Hères, France

Abstract In this paper, we present a model describing the dynamics of a population of ice floes with arbitrary shapes and sizes, which are exposed to atmospheric and oceanic skin drag. The granular model presented is based on simplified momentum equations for ice floe motion between collisions and on the resolution of linear complementarity problems to deal with ice floe collisions. Between collisions, the motion of an individual ice floe satisfies the linear and angular momentum conservation equations, with classical formula applied to account for atmospheric and oceanic skin drag. To deal with collisions, before they lead to interpenetration, we included a linear complementarity problem based on the Signorini condition and Coulombs law. The nature of the contact is described through a constant coefficient of friction μ, as well as a coefficient of restitution ($0 \leq \varepsilon \leq 1$) describing the loss of kinetic energy during the collision. In the present version of our model, this coefficient is fixed. The model was validated using data obtained from the motion of interacting artificial *wood* floes in a test basin. The results of simulations comprising few hundreds of ice floes of various shapes and sizes, exposed to different forcing scenarios, and under different configurations, are also discussed. They show that the progressive clustering of ice floes as the result of kinetic energy dissipation during collisions is well captured, and suggest a collisional regimes of floe dispersion at small scales, different from a large-scale regime essentially driven by wind forcing.

1. Introduction

When considering large scales (>10 km^2) and large sea ice concentrations ($> 80\%$), it is reasonable to use a continuum mechanics description of sea ice [e.g., *Feltham*, 2008], as long as the sea ice rheology used is appropriate [*Girard et al.*, 2011]. Such continuous description facilitates coupling with ocean and atmospheric models. In contrast, when considering small scales ($\simeq 10$ km^2 or less) and/or regions with a lower sea ice concentration, such as the marginal ice zone (MIZ), the discontinuous nature of the ice cover cannot be ignored when considering sea ice mechanics and kinematics. These scales and conditions are important for industrial, shipping, and operational forecasting purposes. Indeed, the decline of Arctic sea ice cover [*Stroeve et al.*, 2012b] had led to a new scramble for territory and resources. If sea ice conditions become less hazardous, some shipping routes may become more negotiable. Moreover, the Arctic is one of the few regions in the world where the hydrocarbon resources are virtually untouched. The decline in sea ice may make it less hazardous to exploit these resources. In this context, improving the accuracy of mechanical models for sea ice is essential, from the aspect of ice/offshore-structure interactions to the aspect of shipping route management and/or operational forecasting. In these conditions, a description in terms of an assembly of individual sea ice floes in mechanical interaction should be favored for an accurate description of the fine-scale structure of sea ice drift and internal forces. The numerical cost of these modeling approaches and the challenges posed by the modeling of floe-floe interactions (collisions) or how they can be combined with atmospheric as well as oceanic continuous models has resulted in them being much less developed so far than continuum mechanic models. The first attempts were proposed by *Hopkins* [1996] and *Hopkins et al.* [2004], and interest was recently renewed by *Herman* [2011] and *Wilchinsky et al.* [2010]. This type of method has also been used at very small scales (<100 m^2) to simulate the formation of ice ridges [*Hopkins*, 1998], or ice/structure interactions [e.g., *Paavilainen et al.*, 2011]. However, these *granular* sea ice models consider simplified floe geometries and are based on a molecular dynamics scheme [*Tsai and McNamara*, 2011]. Thus, these models estimate floe-floe contact forces based on an interpenetration scheme (either linear or Hertzian) which represents a gross approximation if it is applied to a broad range of floe sizes and complex floe geometries. For example, in *Wang and Derradji-Aouat* [2010], ice floes are

squares of the same size; in *Metrikin et al.* [2013], ice floes are quadrangles of different sizes; in *Herman* [2013], ice floes are disks of different sizes; while in *Hopkins et al.* [2004], the model pack was constructed from a Delaunay triangulation. In this last case, as the total surface is initially paved with polygons, the introduction of cohesive forces between the discrete elements allows sea ice fracturing and fragmentation to be described. Hence, the discrete-element method is used as a mathematical representation of the ice pack, and floes of various shapes and sizes can be represented as aggregations of discrete polygonal elements [*Hopkins et al.*, 2004].

Regarding the description of floe/floe collisions, in *Herman* [2013], the normal force at contact is the sum of a Hertzian contact force and a damping force. In Hertzian mechanics, the normal force is null when the distance δ between the edges of the neighboring floes is positive, and scales as $|\delta|^{3/2}$ when $\delta \leq 0$ (interpenetration case). Similarly, the tangential force is the sum of a shear force and a damping force. The Hertzian contact model is suitable for systems consisting of disks or spheres, but is not appropriate for arbitrary contact geometries. *Wang and Derradji-Aouat* [2010] presented a model based on a penalty method and considered contact between bodies as spring and damper systems. The normal force is equal to zero when $\delta > 0$, and increases monotonically as interpenetration increases ($\delta \leq 0$). Typically, the normal force is modeled as a linear spring force $-K\delta$, where K is the spring constant as in the classical molecular dynamics method. Although successfully used to simulate granular flows with many contacts, this method introduces artificial stiffness or heuristic parameters.

The approach we present here is different: we consider the dynamics of assemblies of individual ice floes of any shape and/or size; instead of molecular dynamics, it is based on an event-driven algorithm and particular focus is placed on collisions between floes, while avoiding interpenetration.

Between collisions, the motion of individual floes satisfies the linear and angular momentum conservation equations, with classical formulations for the Coriolis effect as well as atmospheric and oceanic skin drags. To detect future collisions, bounding volume hierarchy algorithms were adapted to our framework, with disks approximating the boundary shapes for the ice floe. To deal with collisions before they lead to interpenetration, a linear complementary problem was written based on the Signorini condition and Coulombs law for frictional contact. In this framework, the normal and tangential impulses are the unknowns, rather than the contact forces as would be the case in molecular dynamics. The nature of the contacts was described through a constant coefficient of friction and a coefficient of restitution describing the loss of kinetic energy during the collision due to damage to and fracturing of the floes in the vicinity of the zone of contact. Each individual floe was meshed with finite elements, allowing a precise description of any floe geometry and of collision scenarios. This precise management of the contacts also minimizes the numerical dispersion and diffusion during simulations. It is worth mentioning here that, at its present stage, our model does not consider ice rheology: floes are purely rigid bodies; that is, do not deform either elastically or inelastically, and kinetic energy dissipation during collisions was described using a purely an empirical parameter.

This paper is organized as follows: section 2 presents our model in detail. First, the motion of a single ice floe is described, then the geometry discretization, followed by the collision detection between ice floes and, finally, collision processing. Section 3 presents how the model was validated using algorithmic, numerical, and experimental data. Section 4 presents the simulations of ice floes drifting across a channel, with various values for the restitution coefficient and the friction coefficient as well as ice floes drifting under varying wind and current in an open ocean. Finally, section 5 concludes the paper.

2. Model

We considered an ensemble of n polygonal ice floes $\{\Omega_1, \ldots, \Omega_n\}$, with, for all $i \in \{1, \ldots, n\}$, masses M_i, centers of mass G_i, and m contact points $\{p_1, \ldots, p_m\}$, with their orthonormal frame:

$$\left\{ \mathcal{R}_{p_1} = (p_1, \mathbf{T}_1, \mathbf{N}_1), \ldots, \mathcal{R}_{p_m} = (p_m, \mathbf{T}_m, \mathbf{N}_m) \right\}$$

where, for all $j \in \{1, \ldots, m\}$, $\mathbf{N}_j$ is directed outward, normal to the surface and $\mathbf{T}_j$ represents the vector tangential to the contact (see Figure 1).

Movement of an ice floe is determined by surface forces: the Coriolis effect, atmospheric and oceanic skin drags, and floe/floe interaction forces. This model has two goals:
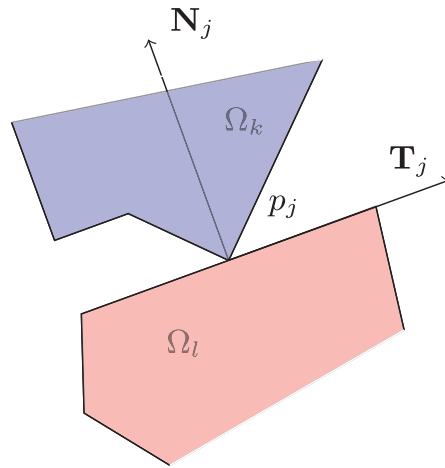
Figure 1. Contact point with its contact frame.

1. To describe the motion of individual ice floes between collisions.
2. To describe floe/floe interactions due to collisions.

The present model treats ice floes as rigid bodies with masses. In our model, the mass M is a linear function of the surface S (m^2) of the ice floe and its thickness h (m) (in the version of the model presented here, h has been set constant over each ice floe). Thus, $M = \rho S h$, where ρ is the ice's density (kg/m^3) (see section 2.3.1).

2.1. External Forces

The dominating forces acting on the surfaces of an ice floe are the result of atmospheric and oceanic skin drags. Our model is built as a sea-ice only model that is not coupled dynamically or thermodynamically to the ocean. We wrote these atmospheric and oceanic skin drags per unit area τ_a and τ_w, respectively, on a classical quadratic form [*McBean*, 1986; *McPhee*, 1986].

$$\tau_a = \rho_a C_a ||\mathbf{u}_a|| \mathbf{u}_a$$

$$\tau_w = \rho_w C_w ||\mathbf{u}_w - \mathbf{V}|| (\mathbf{u}_w - \mathbf{V})$$

where $\mathbf{u}_a$, $\mathbf{u}_w$, and $\mathbf{V}$ are the air velocity, water velocity, and ice floe velocity, respectively. The Coriolis effect, $\mathfrak{F}_c$, acts perpendicularly to the center of mass motion, such that $\mathfrak{F}_c = -f\mathbf{k} \wedge \mathbf{V}$, where f is the Coriolis parameter and $\mathbf{k} = (0, 0, 1)^T$ is a vector pointing vertically upward. The different constants and parameters of the model are given in Table 1.

With this quadratic ocean drag formulation, the ocean current acts as a force on the ice floe surface, but drifting floes do not affect the ocean boundary layer. The coupling between the population of ice floes and the oceanic boundary layer is left for future work.

2.2. Momentum Equations

Between collisions, the motion of the ith ice floe Ω_i satisfies the linear momentum conservation equation and the angular momentum conservation equation:

$$\mathbf{M}_i \frac{d\mathbf{V}_i}{dt} = M_i \mathfrak{F}_c + \int_{\Omega_i} \tau_a + \tau_w \quad \text{linear momentum}$$

$$I_i \frac{d\omega_i}{dt} = \int_{\Omega_i} \mathbf{r}_{ij} \wedge (\tau_a + \tau_w) \quad \text{angular momentum}$$

(1)

where $\mathbf{M}_i$ is the mass matrix, I_i is the moment of inertia, $\mathbf{V}_i$ is the velocity of center of mass of Ω_i, ω_i is the angular velocity, and $\mathbf{r}_{ij}$ is a vector pointing from the center of mass of the ith ice floe Ω_i, to a mesh point $j \in \Omega_i$.

Table 1. Physical Model Parameters Used in the Simulations

Constant Parameters	Symbol	Value	Units
Earth's angular velocity	V_Ω	7.292×10^{-5}	s^{-1}
Latitude	ϕ	Variable	rad
Coriolis parameter	f	$2V_\Omega \sin \phi$	s^{-1}
Air density	ρ_a	1.341	kg/m^3
Ice density	ρ	917	kg/m^3
Water density	ρ_w	1024.071	kg/m^3
Atmospheric skin drag coefficient	C_a	1.7×10^{-3}	
Oceanic skin drag coefficient	C_w	5×10^{-3}	
Ice floe velocity	$\mathbf{V}$	Variable	m/s
Surface current velocity	$\mathbf{u}_w$	Variable	m/s
Wind velocity	$\mathbf{u}_a$	Variable	m/s
Mesh size	s_m	$S/25$	m^2

2.3. Geometrical Description of the Assembly of Ice Floes

Unlike most of the models previously developed, we considered ice floes of any size and shape. To do so, individual ice floes were discretized with finite elements. Realistic configurations could be retrieved from, e.g., aerial or satellite images (see Figure 2).

2.3.1. Ice Floe Discretization

To discretize each individual ice floe, we used the finite element method (FEM) associated with the three-point Gauss-
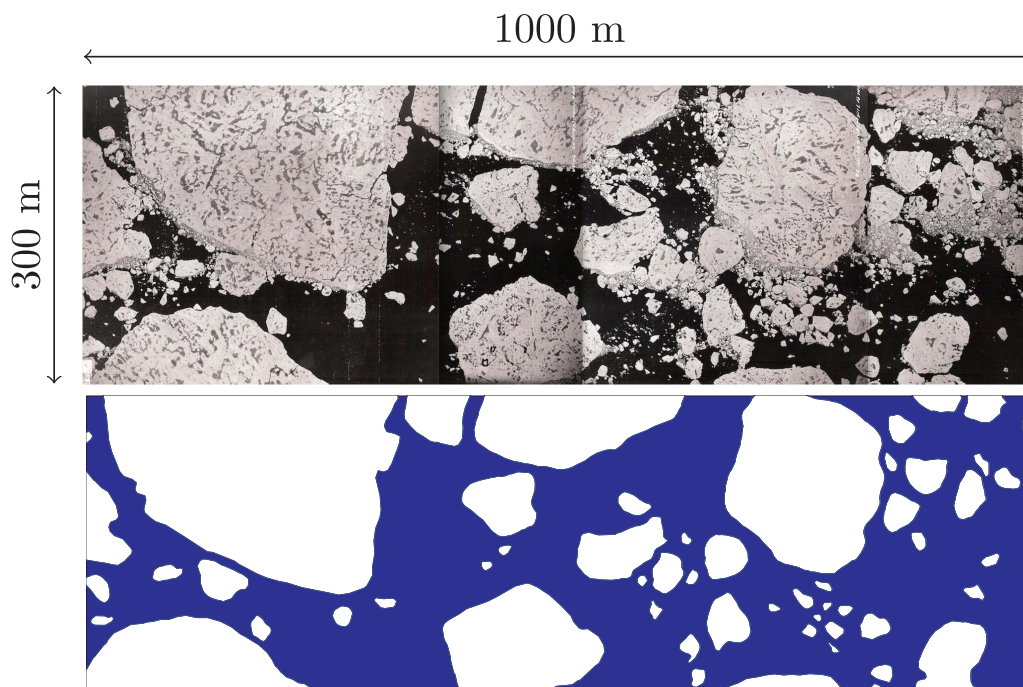
Figure 2. Realistic configuration based on an aerial image of the Roberson channel (Northwest Greenland).

Legendre quadrature method [*Rathod et al.*, 2004]. Thus, external forces were applied to each element of the mesh and the integration of atmospheric and oceanic skin drags can be performed over the whole ice floe area (see equation (1)). The ice floe thickness can vary from one element of the mesh to another for the same floe. However, this possibility was not considered in the present version of our model (h constant over S for each ice floe). As FEM models are generally computationally expensive and as our model aimed to simulate the motion of several thousands of ice floes, we used the following idea: we defined the size of the mesh element s_m, according to the ice floe surface area S (see Table 1). Thus, each floe, whether small or large, was meshed with the same number of finite elements—around 25 per floe. In section 2.4.1, we will see that this leads to a definition of collision based on ice floe size. Oceanic skin drag was applied as an external force on each element of the ice floe mesh (see Figure 3).

2.3.2. Time Discretization

To simulate ice floe motion, we used linear and angular momentum conservation and applied an explicit scheme for temporal discretization. We considered that the mass matrix $\mathbf{M}_i$, and the moment of inertia I_i, to be constant (S_i and h_i do not change over time). In addition, as ice floes are rigid, the vector $\mathbf{r}_{ij}$ is fixed, this produces:

$$\mathbf{M}_i\mathbf{V}_i(t+\Delta t)=\mathbf{M}_i\mathbf{V}_i(t)+\mathbf{M}_i\Delta t\widetilde{\mathfrak{F}}_c(t)+\Delta t\int_{\Omega_i}\tau_a+\tau_w(t)$$

$$I_i\omega_i(t+\Delta t)=I_i\omega_i(t)+\Delta t\int_{\Omega_i}\mathbf{r}_{ij}\wedge(\tau_a+\tau_w)(t)$$

Generally, implicit integration is preferred to ensure stable behavior for any time step. However, in our model, as we have adjusted the time step according to ice floe velocities and the distance between ice floes (see section 2.5), the explicit integration has been chosen. For this integration scheme, to remain stable, the time step should be small. For example, in the simulations detailed in section 4, the time step should not exceed 30 s to ensure stability. Moreover, with the geometric characteristics of the collision zone, there exists a theoretical minimum time step equal to 0.075 s (see section 4.1). This minimum time step is reached when the ice floes enter the collision zone with the maximum (free drift) speed. This case is a rare event. Indeed, as soon as collisions occur, the speed decreases due to the restitution coefficient <1 and so the time step increases again. In the simulation of section 4, the minimum time step was around 0.1 s and the average was around 3.5 s.
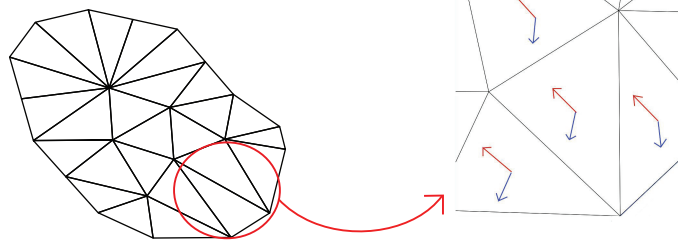
Figure 3. Ice floe meshed with external forces applied on each element of the mesh.

2.4. Modeling Ice Floe Interactions

Our model is based on an event-driven algorithm [*McNamara*, 2011]. To deal with collisions, we started by a detection stage. First, the minimum distance δ_{ij}, between two ice floes Ω_i and Ω_j for all pairs (i, j), where $i \neq j \in \{1, \dots, n\}$, was computed. Then, knowing ice floe velocities and positions, an estimation of future position was made. This made it possible to predict the potential contact points and the time step could be adjusted to avoid interpenetration. Finally, we built the contact frames associated with each contact point (see Figure 1). Then, in a second step, we dealt with the collisions obtained from the previous step. This consisted in writing a linear complementarity problem (LCP) [*Cottle et al.*, 1992] with constraints derived from the geometrical data relating to collisions. These constraints are: a noninterpenetration constraint and a friction constraint based on Coulomb friction. In this framework, the normal and tangential impulses are the unknowns (see section 2.4.2).

2.4.1. Collision Detection

The collision detection problem has been extensively studied over the last few decades. A multitude of algorithms have been proposed to deal with this problem. Some are based on the extrusion operation [*Cameron*, 1990], others on the spatial partitioning representations [*Hadama and Hori*, 1996], or on bounding volume hierarchies (BVH) [*Quinlan*, 1994; *Hamlin et al.*, 1992]. We adapted the BVH algorithm to our framework using disks to approximate the ice floe shapes. The disks were described by their center and radius.

We built two levels of disks. The ensemble of level 1 disks entirely covers the mesh border of the ice floe and the associated collision zone $\mathcal{Z}$. This collision zone serves to define the contact between two ice floes (see below). Moreover, the center of each level 1 disk is a vertex of the ice floe border mesh and the radius of each disk can be different. The level 0 disk covers all the level 1 disks (see Figures 4 and 5). Level 0 and level 1 disks are noted $\mathcal{D}^0$ and $\mathcal{D}^1$, respectively.

The levels of disks were built based on two concepts: the collision zone $\mathcal{Z}$ and the threshold distance η. We started by defining the threshold distance. η is defined according to the surface area S of the ice floe, $\eta = \sqrt{S}/100$. Then, we defined the collision zone $\mathcal{Z}$ associated with ice floe Ω. $\mathcal{Z}$ is the set of points p, such that $p \notin \Omega$, and the minimum distance between p and Ω is smaller than η (see Figure 5).

Let $\mathcal{Z}_i$ and $\mathcal{Z}_j$ be the collision zones associated with Ω_i and Ω_j, respectively. Collision between Ω_i and Ω_j occurs if and only if $\mathfrak{C}_j \cap \mathcal{Z}_i \neq \varnothing$ or $\mathfrak{C}_i \cap \mathcal{Z}_j \neq \varnothing$, where $\mathfrak{C}_i$ $\mathfrak{C}_j$ is the set of vertices of the mesh border of Ω_i Ω_j. If $\mathfrak{C}_i \cap \mathcal{Z}_j \neq \varnothing$ then there exists a point $p \in \mathfrak{C}_i$ such that $p \in \mathcal{Z}_j$. In this case, p is called a contact point and the set of contact points belonging to ice floe Ω_i is denoted $\mathcal{P}_c^i$. The main property of the level 1 disks is that if $p \in \Omega_i$ is a contact point, then at least one disk $\mathcal{D}_j^1$ of the level 1 of Ω_j exists such that $p \in \mathcal{D}_j^1$.

The algorithm used to compute the minimum distance δ_{ij}, between two ice floes Ω_i and Ω_j, such that $\mathcal{D}_i^0 \cap \mathcal{D}_j^0 \neq \varnothing$ is presented in Figure 6. The overlap of the level 0 disks between Ω_i and Ω_j was denoted $\mathcal{O}_{ij}$. First, we checked, for all level 1 disks for the two floes, whether the disk belonged to the overlap $\mathcal{O}_{ij}$. Then, we selected the points along the mesh border for these level 1 disks and tested whether they belonged to the collision zone. Thus, we computed the minimum distance $d(p_i, \Omega_j)$, between a point $p_i \in \mathfrak{C}_i \cap \mathcal{D}_j^1$ and the other floe Ω_j. Finally, the minimum distance between two ice floes Ω_i and Ω_j could be defined by:

$$\delta_{ij} = \min_{\substack{p_i \in \mathcal{P}_i^c \\ p_j \in \mathcal{P}_j^c}} \left(d(p_i, \Omega_j), d(p_j, \Omega_i) \right)$$

Then, for each contact point p, we determined the contact frame $\mathcal{R}_p = (p, \mathbf{T}_p, \mathbf{N}_p)$ (see Figure 1). To build $\mathcal{R}_p$, we first define the normal $\mathbf{N}_p$, directed outward to the surface at p. Considering any shapes, there exists
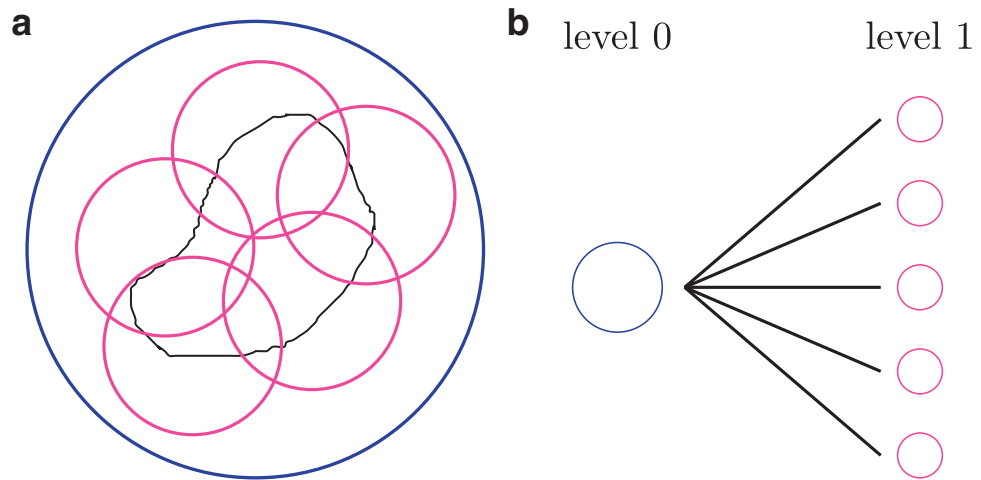
Figure 4. Bounding hierarchy.

configurations where the normal to the surface is ill defined. An example is a convex corner, whereas for a concave corner the normal is the null vector. This kind of configuration occurs in cases where the contact is *node to node*. When contact is *node to segment*, the normal $\mathbf{N}_p$ is well known as the normalized vector equal to $\mathbf{pq}'$, where $q' \in \Omega$ such that $d(p, \Omega) = d(p, q')$ and $d(p, q')$ is a Euclidean distance between points p and q'. In the case *node to node*, we defined the normal $\mathbf{N}_p$, as the normalized vector equal to $\mathbf{pq}$ where $q \in \mathfrak{C}$ such that $d(p, \Omega) = d(p, q)$ (see Figure 7).

2.4.2. Collision Processing

In simulations of multibody rigid dynamics based on the Coulomb friction model, it is impossible to accurately describe how the contact forces change during contact. Indeed, during contact many complex and brief interactions occur between the bodies. It is therefore common to consider the collision time as infinitesimally small. Thus, we considered that over the collision time interval, the integrals of the external forces, called impulses, to be negligible except for the contact forces. Collisions are rapid events characterized by large contact forces, we therefore considered the impulse of a contact force to be a finite quantity $\mathcal{I}$.

The problem of multiple contacts where the unknowns are the impulses was first studied by *Delassus* [1917]. Later, Moreau proposed an approach based on a linear complementarity problem [*Moreau*, 1963; *Pfeiffer and Glocker*, 1996]. More recently, several extensions and proofs of existence and convergence have been proposed [*Stewart and Trinkle*, 1996; *Stewart*, 2000; *Anitescu and Potra*, 1997; *Anitescu et al.*, 1999]. We solved this linear complementarity problem using Lemke's algorithm [*Cottle et al.*, 1992, Alg. 6.3.1] and the impulses found made it possible to determine the ice floes velocities after the contact.
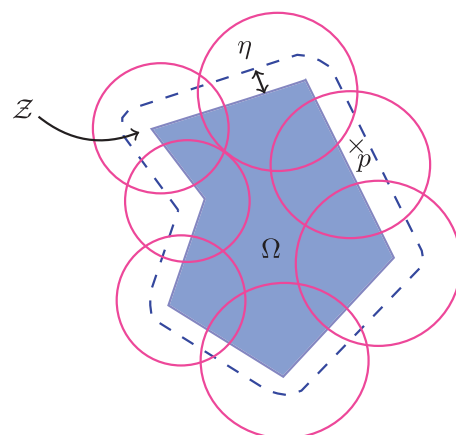

Figure 5. Level 1 disks.

The impulse applied to Ω_k due to a contact at point p_j was denoted $\mathcal{I}_{kj}$, while the collision time interval was denoted $[t^* - \xi, t^* + \xi]$, where $\xi \to 0$. The momentum equations for the motion of ice floe Ω_i can therefore be written as follows:

$$\mathbf{M}_i \mathbf{V}_i(t^+) = \mathbf{M}_i \mathbf{V}_i(t^-) + \sum_{j \in P_c^i} \mathcal{I}_{ij}$$

$$I_i \omega_i(t^+) = I_i \omega_i(t^-) + \sum_{j \in P_c^i} \mathbf{r}_{ij} \wedge \mathcal{I}_{ij} \qquad (2)$$

where $t^+ = \lim_{\xi \to 0} (t^* + \xi)$ and $t^- = \lim_{\xi \to 0} (t^* - \xi)$

The decomposition of $\mathcal{I}_{kj}$ into $\mathcal{R}_{p_j}$ was noted (β_j, λ_j). β_j is called the tangential contact impulse and λ_j is called the normal contact impulse. We built two matrices $\mathbf{D} \in \mathbb{R}^{3n \times m}$ and $\mathbf{J} \in \mathbb{R}^{3n \times m}$, containing the coordinates of the normal
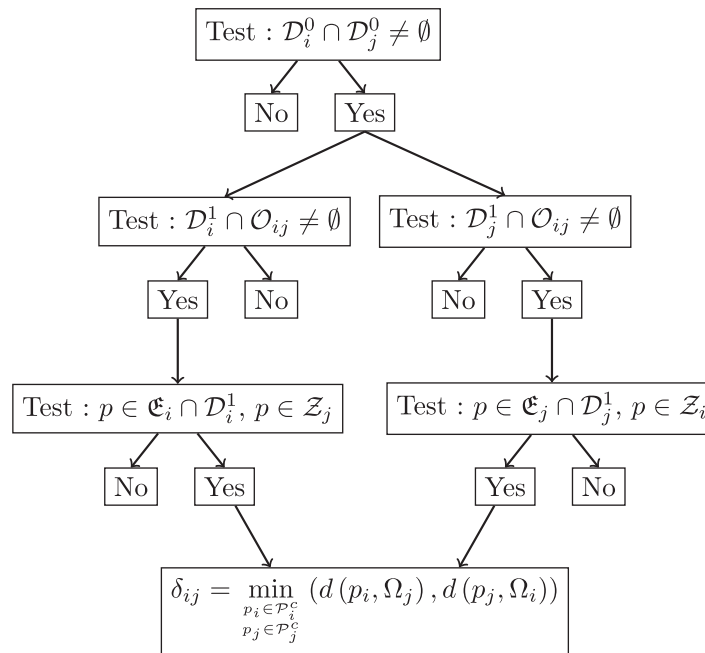
Figure 6. Algorithm used to compute the minimum distance between Ω_i and Ω_j.

and the tangent of the contacts, respectively. Matrices **D** and **J** satisfy the two following properties:

$$(i) \forall j \in \{1, \ldots, m\}, \mathbf{D}_{(k,j)}\beta_j + \mathbf{J}_{(k,j)}\lambda_j = \begin{pmatrix} \mathcal{I}_{kj} \\ \mathbf{r}_{kj} \wedge \mathcal{I}_{kj} \end{pmatrix}$$

$(ii) \forall j \in \{1, \ldots, m\}, p_j$ is associated with (Ω_l, Ω_k),

$$(\mathbf{D}^T)_{(j;\{l,k\})} \begin{pmatrix} \mathbf{V}_l \\ \omega_l \\ \mathbf{V}_k \\ \omega_k \end{pmatrix} = \mathbf{v}_j^R . \mathbf{T}_j$$

$$\text{and } (\mathbf{J}^T)_{(j;\{l,k\})} \begin{pmatrix} \mathbf{V}_l \\ \omega_l \\ \mathbf{V}_k \\ \omega_k \end{pmatrix} = \mathbf{v}_j^R . \mathbf{N}_j$$

where $\mathbf{v}_j^R$ is the relative velocity of contact point $p_j \in \Omega_l$ in the frame associated with Ω_k.

Combining equation (2), we can write the following system for ice floe Ω_i:

$$\begin{pmatrix} \mathbf{M}_i & 0 \\ 0 & I_i \end{pmatrix} \begin{pmatrix} \mathbf{V}_i \\ \omega_i \end{pmatrix} (t^+) = \begin{pmatrix} \mathbf{M}_i & 0 \\ 0 & I_i \end{pmatrix} \begin{pmatrix} \mathbf{V}_i \\ \omega_i \end{pmatrix} (t^-) + \sum_{j \in P_c^i} \mathbf{D}_{(i,j)}\beta_j + \mathbf{J}_{(i,j)}\lambda_j \tag{3}$$

Then, we can combine this equation (3) for each ice floe to obtain a global system:

$$\mathbf{MW}(t^+) = \mathbf{J}\lambda + \mathbf{D}\beta + \mathbf{MW}(t^-) \quad \in \mathbb{R}^{3n} \tag{4}$$
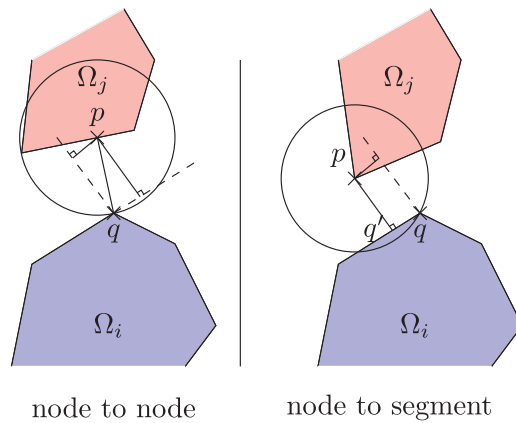
where

$$\mathbf{M} = \begin{pmatrix} \mathbf{M}_i & 0 \\ 0 & I_i \end{pmatrix}_{1\leq i\leq n}, \quad \mathbf{W} = \begin{pmatrix} \mathbf{V}_i \\ \omega_i \end{pmatrix}_{1\leq i\leq n}$$

and

$$\lambda = (\lambda_j)_{1\leq j\leq m}, \quad \beta = (\beta_j)_{1\leq j\leq m}$$

where the ice floe velocities after collisions $\mathbf{W}(t^+)$, and the impulses λ and β are the unknowns. To determine the ice floe velocities after collision, we added two complementarity constraints to the system 4: a noninterpenetration constraint and a friction constraint.

Figure 7. Possible contact configurations.

We refer to the Signorini condition [*Signorini*, 1933] to establish the noninterpenetration constraint. Signorini studied an elastic body which is unilaterally supported by a rigid foundation. He looked for a displacement field which is a state of equilibrium with a body force. This physical situation can be expressed by the classical unilateral boundary conditions of the Signorini type:

$$u_n \leq 0, \quad F_n \leq 0, \quad u_n . F_n = 0 \text{ on } \Gamma$$

where u_n and F_n denote the normal components of displacements and stresses, respectively, and Γ denotes the rigid foundation. For our noninterpenetration constraint, instead of establishing a link between displacements and stresses, we make a link between the relative velocities and impulses. Specifically, we made a link between the normal contact impulse λ_j, applied to the contact point p_j, and the normal relative velocity $\mathbf{v}_j^R.\mathbf{N}_j$, of p_j. First, as contacts were only associated with compressive forces (no cohesion between ice floes), we have $\lambda_j \geq 0$. Second, as there is no interpenetration, we have $\mathbf{v}_j^R.\mathbf{N}_j \geq 0$. In case of takeoff, we have $\mathbf{v}_j^R.\mathbf{N}_j > 0$ and no contact force $\lambda_j = 0$. In case of adhesion, we have $\mathbf{v}_j^R.\mathbf{N}_j = 0$ and a nonzero normal contact impulse $\lambda_j > 0$. These conditions generate a complementarity condition for each contact point p_j, and we can write an overall complementarity condition:

$$\mathbf{w} = \mathbf{J}^T \mathbf{W}(t^+) \geq 0, \quad \lambda \geq 0, \quad \mathbf{w}^T.\lambda = 0 \quad (5)$$

To describe friction, we need to know the direction of slip. In the 2-D case, for each contact point p_j, there are only two possible directions: $\mathbf{T}_j$ or $-\mathbf{T}_j$. We based our complementarity condition on the work of *Stewart and Trinkle* [1996] which establishes a link between the tangential contact impulse β_j, applied to contact point p_j, the normal contact impulse λ_j, the tangential relative velocity $\mathbf{v}_j^R.\mathbf{T}_j$, of p_j and the friction coefficient μ, as follows:

$$\begin{cases} \gamma_j = \begin{pmatrix} \mathbf{v}_j^R.\mathbf{T}_j \\ -\mathbf{v}_j^R.\mathbf{T}_j \end{pmatrix} + \alpha_j \begin{pmatrix} 1 \\ 1 \end{pmatrix} \geq 0, \quad \tilde{\beta}_\mathbf{j} \geq 0, \quad \gamma_j^T.\tilde{\beta}_j = 0 \\ \sigma_j = \mu\lambda_j - \begin{pmatrix} 1 \\ 1 \end{pmatrix}^T \tilde{\beta}_j \geq 0, \qquad \alpha_j \geq 0, \quad \sigma_j^T.\alpha_j = 0 \end{cases}$$

where α_j can be seen as an approximation of the magnitude of the relative contact velocity and $\tilde{\beta}_j$ is a vector containing the component for each direction $\mathbf{T}_j$ and $-\mathbf{T}_j$ of the tangential contact impulse.

These complementarity constraints behave like the Coulomb friction model. Indeed, if $\mu\lambda_j - (1,1)\tilde{\beta}_j > 0$; that is, the contact impulse is inside the Coulomb cone, then $\alpha_j = 0$ and therefore $\left(\mathbf{v}_j^R.\mathbf{T}_j, -\mathbf{v}_j^R.\mathbf{T}_j\right)^T \geq 0$. Hence, the tangential relative velocity is zero.

In contrast, when $\mu\lambda_j - (1,1)\tilde{\beta}_j = 0$, then there exists a direction $\mathbf{d}_{slip} \in \{\mathbf{T}_j, -\mathbf{T}_j\}$, such that the component of the tangential contact impulse associated with this direction β_j is strictly positive. Therefore, $\alpha_j + \mathbf{v}_j^R.\mathbf{d}_{slip} = 0$. For $\alpha_j \neq 0$, we have $\beta_j \mathbf{v}_j^R.\mathbf{d}_{slip} < 0$, causing the friction force to exhibit negative work, as expected. Therefore, in the other direction $-\mathbf{d}_{slip}$, $\alpha_j - \mathbf{v}_j^R.\mathbf{d}_{slip} > 0$, the component of the tangential contact impulse associated with this direction will be zero.

We can write this type of friction condition for each contact point to generate a global complementarity condition:

$$\begin{cases} \gamma = \mathbf{D}^T\mathbf{W}(t^+) + \mathbf{H}\alpha \geq 0, & \tilde{\beta} \geq 0, & \gamma^T.\tilde{\beta} = 0 \\ \sigma = \mu\lambda - \mathbf{H}^T\tilde{\beta} \geq 0, & \alpha \geq 0, & \sigma^T.\alpha = 0 \end{cases} \tag{6}$$

where

$$\mathbf{H}^T = \left(e_{ij}\right)_{\substack{1 \leq i \leq m, \\ 1 \leq j \leq 2m}}, \quad \tilde{\beta} = \left(\tilde{\beta}_j\right)_{1 \leq j \leq m}$$

$$e_{ij} = \begin{cases} 1 & \text{if} \quad j = 2(i-1)+1 \text{ or } j = 2(i-1)+2 \\ 0 & \text{otherwise} \end{cases}$$

It is not straightforward to determine the tangential impulse. Indeed, Coulombs friction model gives a local relationship between the tangential and the normal impulse, meaning that this model describes the contact behavior for only one contact point; this is not sufficient to describe the overall behavior. Indeed, the contact behaviors of all contact points taken individually are not sufficient to describe the motion of a group of floes in interaction with each other, as this depends on the overall floe configuration. For this reason, we deal with all contact points p_j, for all $j \in \{1, \ldots, m\}$, simultaneously. This is an approximation to reality. Indeed, in the case of contact chains, e.g., the Newton's cradle problem, we have to be careful with the temporal consistency (see section 3.1.2). Another method is to consider only the contact points leading to an interpenetration, i.e., the points $p_j \in I_n(t)$, where $I_n(t) = \{\forall j \in \{1, \ldots, m\}, p_j / v_j^R.N_j(t) < 0\}$. At step 0, we deal with the contact points belonging to $I_n^0 = I_n(t^-)$ with the two constraints (noninterpenetration and Coulomb's friction). We continue this process while $I_n \neq \varnothing$, i.e., until step r, such that $I_n^r = I_n(t^+) = \varnothing$. The treated contact points at step k satisfy the Signorini constraint. Therefore, they do not belong to I_n^{k+1}. However, contact points that do not belong to I_n^k can belong to I_n^{k+1}. The main drawback of this method is that the termination of this iterative process remains an open question [*Smith et al.*, 2012]. Nevertheless, this iterative process terminated for all the simulations performed in this work. In section 4.2, we describe simulation results obtained for the drifting configuration (2) using the two methodologies: dealing with contact points simultaneously, or not. Particularly, we describe the floe trajectories and we show that when dealing with only contact points leading to an interpenetration with the iterative process above, the floe trajectories remain close to that obtained with the first methodology.

From equation (4) and the two complementarity constraints (5) and (6) we can write the linear complementarity problem as follows:

$$\begin{cases} \begin{pmatrix} \mathbf{w} \\ \gamma \\ \sigma \end{pmatrix} = \begin{pmatrix} \mathbf{J}^T\mathbf{M}^{-1}\mathbf{J} & \mathbf{J}^T\mathbf{M}^{-1}\mathbf{D} & 0 \\ \mathbf{D}^T\mathbf{M}^{-1}\mathbf{J} & \mathbf{D}^T\mathbf{M}^{-1}\mathbf{D} & \mathbf{H} \\ \mu & -\mathbf{H}^T & 0 \end{pmatrix} \begin{pmatrix} \lambda \\ \tilde{\beta} \\ \alpha \end{pmatrix} + \begin{pmatrix} \mathbf{J}^T\mathbf{W}(t^-) \\ \mathbf{D}^T\mathbf{W}(t^-) \\ 0 \end{pmatrix} \\ \\ \begin{pmatrix} \mathbf{w} \\ \gamma \\ \sigma \end{pmatrix} \geq 0, \begin{pmatrix} \lambda \\ \tilde{\beta} \\ \alpha \end{pmatrix} \geq 0, \begin{pmatrix} \mathbf{w} \\ \gamma \\ \sigma \end{pmatrix}^T . \begin{pmatrix} \lambda \\ \tilde{\beta} \\ \alpha \end{pmatrix} = 0 \end{cases} \tag{7}$$

We use a restitution coefficient denoted $\varepsilon \in [0, 1]$ to describe the dissipation of kinetic energy during a collision. The contact can be inelastic with little or no bounce and extensive loss of kinetic energy, or elastic with considerable bounce and little or no loss of kinetic energy. For $\varepsilon = 0$, the contact is purely inelastic while for $\varepsilon = 1$, the contact is purely elastic. Different approaches can be used to apply the restitution coefficient, e.g., Newton's law or Poisson's law. Newton's law defines ε as equal to the ratio between the normal relative

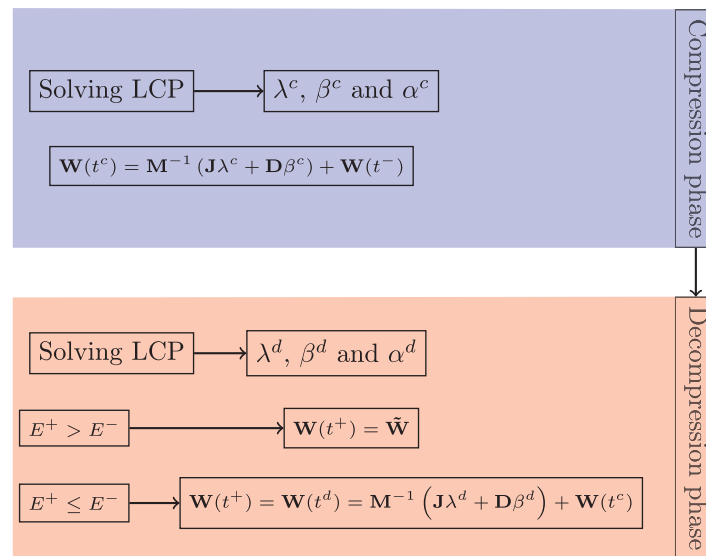**Figure 8.** Collision processing algorithm.

velocity at a contact point before and after a collision, i.e., for a contact point p_j, $|v_j^R.N_j(t^+)|=\varepsilon|v_j^R.N_j(t^-)|$. In contrast, Poisson's law considers that collisions have two phases: a compression phase and a decompression phase, and establishes a relationship between the normal contact impulse in the decompression phase λ^d, and the normal contact impulse in the compression phase λ^c

$$\lambda^d = \varepsilon\lambda^c$$

We opted to use Poisson's law. We will see later that this option makes it possible to establish the existence of a solution for the two phases. In addition, for the compression phase, the solution does not lead to an increase in kinetic energy.

We established a linear complementarity problem (LCP) (7) for each phase. After solving the LCP for the compression and the decompression phases, we computed the ice floe velocities after the compression and the decompression phases $\mathbf{W}(t^c)$ and $\mathbf{W}(t^d)$, respectively. With this computing scheme, the kinetic energy after the decompression phase E^d is not always smaller than the kinetic energy before collision E^-, which is a physical impossibility. In this case, we compute the ice floe velocities using this following equality:

$$\tilde{\mathbf{W}} = (1+\varepsilon)\mathbf{W}(t^c) - \varepsilon\mathbf{W}(t^-) \qquad (8)$$

The solution given by $\tilde{\mathbf{W}}$ does not satisfies the Coulomb's law meaning that a sliding contact might become a rolling contact or vice versa. However, this solution ensures the noninterpenetration between the ice floes; hence, a contact cannot become a sliding contact if this leads to interpenetration. Moreover, this solution ensures that kinetic energy is not increased after the collision. We chose this solution to give priority to the conservation of kinetic energy. This collision processing is summarized in Figure 8.

At the end of the collision processing, the normal component of the relative velocities of the contact point is $w=J^T.W(t^+)$. For two ice floes Ω_i and Ω_k in contact at the contact point p_j, either $w(j)>0$, meaning that the contact is broken and we have a takeoff case, or $w(j)=0$; that is, the two ice floes remain in contact and the ice floes may slid against each other, i.e., $v_j^R.T_j \neq 0$. The configuration (sliding or takeoff) remains unchanged over the time interval $[t^+, t^+ + \Delta t]$ where $\Delta t > 0$ (see section 2.5). At the time $t^+ + \Delta t$, the contact is dealt with again and a new relative normal velocity $w(j)$ is computed. So, the contact can persist over time.

2.5. Main Algorithm

At initial time $t = 0$, we assume that there is no interpenetration between ice floes. The main algorithm for our model is presented in Figure 9 and described below. The first two stages of this algorithm have been previously described (see sections 2.4.1 and 2.4.2). After the collision processing stage and knowing their center of mass and angular velocities, it is easy to compute the appropriate time step to avoid interpenetration between ice floes. For all Ω_i, we built the time step Δt_i, such that the maximal distance traveled by Ω_i during this time step would be smaller than $\delta_{ij}/2$ for all $\Omega_j, j \neq i$.

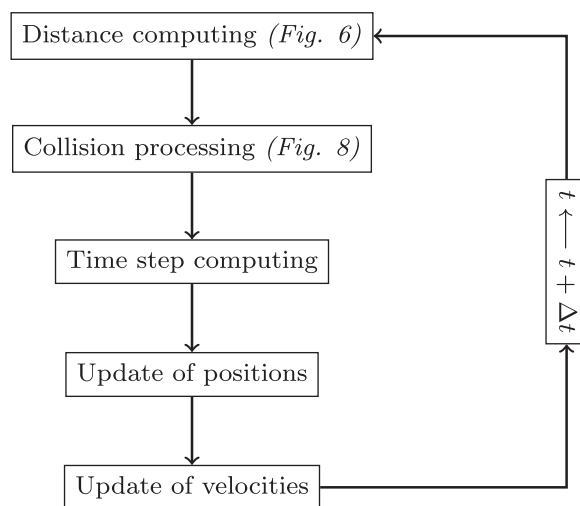From the time steps associated with ice floes, we defined the time step Δt, as follows:

Figure 9. Main algorithm.

$$\Delta t = \min_{i \in \{1,\dots,n\}} \Delta t_i$$

In the case of a collision between Ω_i and Ω_j, we do not need to use the minimum distance δ_{ij}. Indeed, the motion of the contact points cannot lead to interpenetration based on the Signorinis condition (see section 2.4.2). Therefore, we selected the time step Δt_i, such that the maximal distance traveled by Ω_i during this time step would be smaller than $\min(\eta_i, \eta_j)/2$.

3. Model Validation

To validate our model and particularly the collision algorithm, a two-step strategy was used. First, we tested our model with typical collision scenarios, e.g., Bernoulli's problem, Newton's cradle, or the sliding box. This made it possible to verify that our model respects different classical conditions for collisions, such as: preservation of symmetry, no increase in kinetic energy, *break away* (ice floes that were previously in contact may break away from each other as a result of impact) and friction satisfies Coulomb's model. The various tests are presented in section 3.1. We next tested our model using measurements taken in a test basin where pieces of wood with a circular shape were substituted for ice floes.

3.1. Algorithm Validation

After the compression phase, the ice floe velocities found using the LCP satisfied the property of no increase in kinetic energy. However, after the decompression phase, configurations existed where this property was not satisfied. When this was the case, we computed the ice floe velocities using equation (8), which ensures that there will be no increase in kinetic energy.

For the other conditions, we tested our model with classical collision scenarios (see sections 3.1.1–3.1.3). The numerical tests detailed below were performed without Coriolis effect, atmospheric or oceanic skin drags.

3.1.1. Bernoulli's Problem
To test for symmetry conservation, we validated our model against the Bernoulli problem. This problem consists in simulating the collision between three balls B_1, B_2, and B_3 on the plane where B_2 and B_3 are initially at rest and B_1 has an initial velocity $\mathbf{v}_1$, along the symmetry line directed toward B_2 and B_3 (see Figure 10). θ is the angle formed by the mass centers of the balls at the moment of collision.
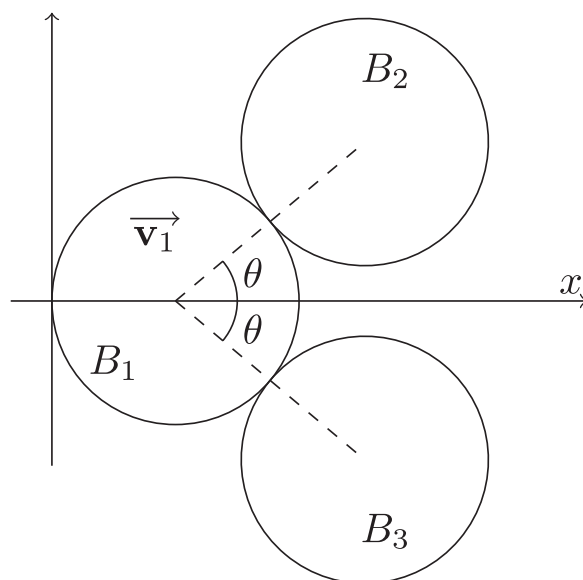
The configuration of the test was as follows: the B_1 velocity was $\mathbf{v}_1 = (1, 0)^T$ m/s, the ball mass was $m = 1$ kg, and the restitution coefficient was the same for all contact points, $\varepsilon = 1$. We focused on the evolution of velocities with an angle θ. Theoretical results are presented in *Liu et al.* [2008] for a frictionless and Hertzian contact between balls. As our model is different from the Hertz model, we obtained
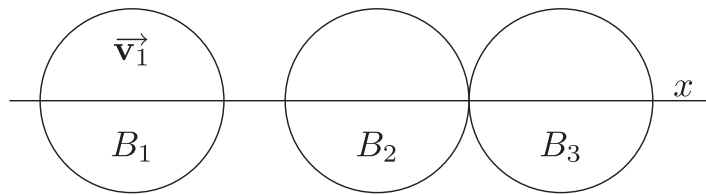

Figure 10. Bernoulli's problem.

Figure 11. Newton's cradle problem.

different results. However, the symmetry is preserved; that is, the trajectories of B_2 and B_3 are symmetric. Moreover, for $\theta = \pi/4$, we obtained the same results as with the Hertz model: $\mathbf{v}_1(t^+) = (0,0)^T$, $\mathbf{v}_2(t^+) = (0.5, 0.5)^T$, and $\mathbf{v}_3(t^+) = (0.5, -0.5)^T$. For $\varepsilon \neq 1$, we observed that the configuration was still symmetric.

3.1.2. Newton's Cradle

To investigate shock propagation, we focused on the Newton's cradle problem. This is one of the simplest multiimpact problems that could be considered. It consists in simulating the collision between three identical aligned balls B_1, B_2, and B_3 where B_2 and B_3 are initially at rest and B_1 has an initial velocity $\mathbf{v}_1$ along the alignment (see Figure 11).

Many studies have been performed to describe the dynamic behavior of the balls during this collisional scenario [see e.g., *Nguyen and Brogliato*, 2014]. The results of these studies showed that the conservation of linear and angular momentum, as well as of kinetic energy, is not sufficient to allow a comprehensive description of the dynamics of the Newton's cradle problem. Indeed, the dynamics of a chain of balls involves two main collisional phenomena: energy dissipation and dispersion. Dissipation is due to plasticity or damage at the contact points. Our model takes dissipation into account through the restitution coefficient ε, but does not consider dispersion, which is due to vibrational and wave effects throughout the whole chain.

The configuration of the test was as follows: the B_1 velocity was $\mathbf{v}_1 = 1$ m/s, the ball mass was $m = 1$ kg, and the restitution coefficient was the same for all contact points, $\varepsilon = 1$. There exists an infinity of solutions for ball velocities after collisions, between (1) $\mathbf{v}_1(t^+) = 0$, $\mathbf{v}_2(t^+) = 0$, and $\mathbf{v}_3(t^+) = 1$ and (2) $\mathbf{v}_1(t^+) = -1/3$, $\mathbf{v}_2(t^+) = 2/3$, and $\mathbf{v}_3(t^+) = 2/3$ [*Nguyen and Brogliato*, 2014]. The solution obtained depends on the energy dispersion. The first solution corresponds to the case of zero dispersion; that is, all the kinetic energy of B_1 is transferred to B_3 after the collision. The second solution corresponds to the case of maximum dispersion.
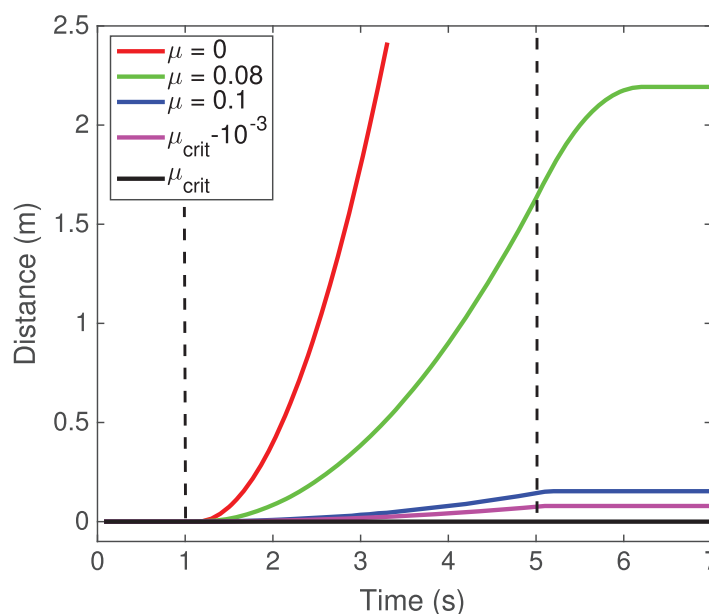

Figure 12. Results for the sliding box scenario, for different values of the friction coefficient.

As stated in section 2.4.2, we dealt with all contact points p_{jr} for all $j \in \{1, \ldots, m\}$, simultaneously. In the Newton's cradle problem, this means that the contacts between balls B_1 and B_2 in one hand and between B_2 and B_3 on the other hand are dealt with together. This means that we did not take into account that the shock propagation starts by the contact between B_1 and B_2 and extends to the contact between B_2 and B_3. This approximation ensures the existence of a solution for the linear complementarity problem (7) and takes into account accurately the Coulomb's friction (see section 2.4.2). This way we obtained a unique solution of the Newton's cradle problem, i.e., the solution
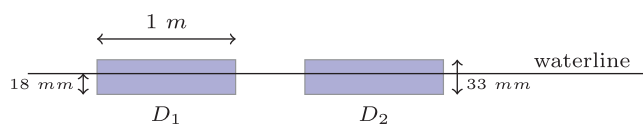
Figure 13. Profile view of the setup used for collision tests between D_1 and D_2.
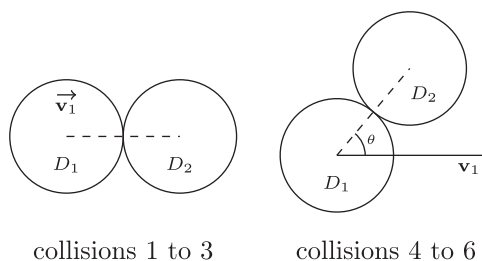

collisions 1 to 3   collisions 4 to 6

Figure 14. Test configurations.

(2) $\mathbf{v}_1(t^+) = -1/3$, $\mathbf{v}_2(t^+) = 2/3$, and $\mathbf{v}_3(t^+) = 2/3$ corresponding to the case of the maximum dispersion. To capture another solutions such as the solution (1) corresponding to zero dispersion, we should take into account the temporal consistency, i.e., dealing with the contact between B_1 and B_2 independently and before the contact between B_2 and B_3.

3.1.3. Sliding Box

To validate our model's handling of frictional collision, we focused on a sliding box scenario. This collision scenario consists in simulating the motion of a box, initially at rest, pushed across a plane. We used a similar configuration to that used by *Drumwright and Shell* [2011]: from $t = 1$ s to $t = 5$ s, a 1 N force parallel to the plane was applied to the box, the box is a square (1 m^2) of unit mass (1 kg), the acceleration due to gravity was $\mathbf{g} = 9.81$ m/s^2, and the restitution coefficient was 0.

Unlike *Drumwright and Shell* [2011], we tested different friction coefficients (see Figure 12). Coulomb's model states that, for this configuration, the friction coefficient from which the unit box starts to move is $\mu_{crit} = 1/9.81$. The results obtained for different friction coefficients are presented in Figure 12 and show that Coulomb's model is obeyed.

3.2. Experimental Validation

We validated our model based on collision experiments performed in a test basin. These experiments consisted in collisions between two identical disks of wood D_1 and D_2 with the same weight 14 kg, in the absence of wind and current (see Figure 13). They consisted in pushing one disk toward the other disk, which was initially floating at rest and repeating this a number of times to explore different conditions. Nine collisions were performed and their effects were recorded with a camera. Image processing was performed to extract the positions and velocities of the mass centers of the two disks as a function of time, according to *Dumont et al.* [2013]. In collisions 1–3, D_1 was pushed toward the mass center of D_2. In collisions 4–6, D_1 was pushed as illustrated in Figure 14. Finally, in collisions 7–9, a significant rotation was induced of D_1 before the collision was effected.

From the initial positions and the initial velocities, we used our model to rebuild the trajectories of the floes. We compared the simulated trajectories (illustrated in red) to the trajectories measured according to *Dumont et al.* [2013] (illustrated in blue). The restitution coefficient was adjusted to minimize the difference between the simulated and extracted trajectories. The best choice was found to be $\varepsilon = 0.35$ and the results presented in Figure 15 are for three different collisions using this value. The agreement between the modeled and the observed trajectories is good, hence our collision modeling scheme is further validated.

4. Simulations

We presented above in full details the structure of the model as well as its validation from simple, well-characterized collisional or frictional scenarios, and from experiments in a test basin. To illustrate the capability of our model to simulate more realistic configurations, we describe below simulation results obtained for two drifting configurations:

1. Ice floes pushed by a constant wind toward a narrow channel (see corresponding movie in supporting information material 1).
2. An assembly of floes drifting in an open ocean under time varying wind and current (see corresponding movie in supporting information material 2).

A more thorough, quantitative analysis of floe drift characteristics for a large population of floes under realistic wind and ocean forcing and with improved coupling with the ocean boundary layer, will be published later.
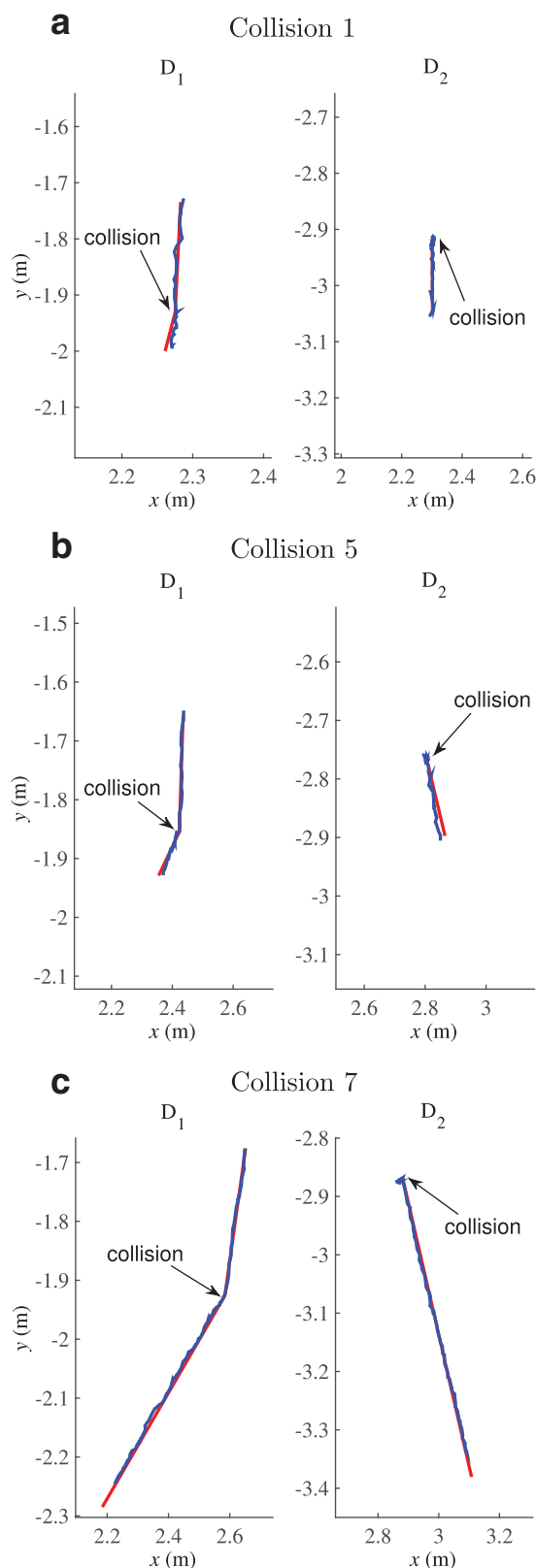
Figure 15. Comparison between simulated trajectories (in red) and measured trajectories (in blue).

4.1. Ice Floes Drifting Across a Channel

For this first configuration, we performed simulations in the following configuration. We used aerial images taken in the Roberson channel (81°N, Northwest Greenland) at the end of summer (see Figure 2). Using image analysis, we generate realistic geometries for 100 ice floes with an area greater than 10 m^2 and with a constant thickness over their surface area $h = 1$ m.

These floes are pushed toward an 850 m width and 2 km long channel by a constant wind with a speed of 10 m/s directed downward at 10° to the vertical (see Figure 16); the ocean is at rest. The simulation time was $T = 5$ h, the maximum time step was $\Delta T = 5$ s, the boundary conditions were two free edges and a channel on either side. The ice floes were initially at rest. The channel played the role of a rigid obstacle, modeled as a body of infinite mass. Tests were performed varying the friction coefficient, the restitution coefficient, and introducing (or not) a Coriolis effect (calculated for a Latitude of 81°N) (see Table 2). The friction coefficient was the same between the ice floes and between the ice floes and the obstacles.

We have previously seen that the time step adapts for each collision to avoid interpenetration of the floes. In the tests presented below, the time step varied between 5 and 0.1 s. This minimum time step was set by the maximum floe speed and the minimum threshold distance η. As the area of the smallest floes was 10 m^2, the minimum value of η was 0.03 m. To avoid interpenetration, ice floes must not move beyond $\eta/2$. With the quadratic form of the external forces and the skin drag coefficients given in Table 1, we obtained a Nansen number equal to 0.021. Thus, the maximum (free drift) speed for ice floes should $\simeq 2\%$ of the wind speed [*Nansen*, 1902; *Weiss*, 2013]. Therefore, the minimum time step was set to 0.075 s.

4.1.1. Qualitative Description

The configurations of the ice floe assembly obtained at two different times for several simulations with different setups are presented in Figures 17–19. In some cases, a proportion of the ice floes remain jammed at the channel's entrance (tests 1, 2, and 5). In tests with a higher restitution coefficient, or a lower friction coefficient, this does not occur (tests 3 and 4). The Coriolis force is generally considered as playing a second-order role on the momentum balance of sea ice [*Hunkins*, 1975], and it might
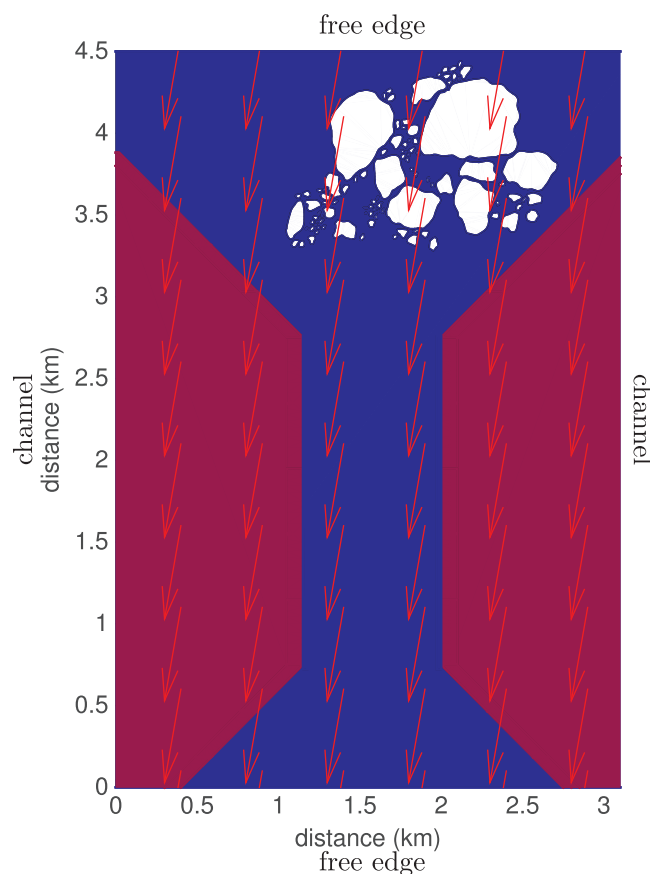
Figure 16. Simulation sketch 3.1.

have been expected to play a negligible role in determining the dynamics of the floe assembly when considering time scales shorter than the inertial period ($\simeq$ 12 h in the Arctic). However and despite the fact that the oceanic skin drag formulation might damp sea ice motion at inertial frequencies (see section 2.1), comparison of the results from tests 1 and 5 revealed significant differences, indicating that the overall dynamics of the floe assembly might be sensitive to small changes in the momentum balance of individual floes, through modification of the collisional scenarios. On Figure 20, we drew the center of mass trajectories for all floes of test number 5.

4.1.2. Quantitative Description

How the total kinetic energy of the floe assembly changes over time is shown in Figure 21. The horizontal black line at the top of the graph represents an upper bound corresponding to a pure free drift for each individual floe, at a speed of about 2% of the wind speed. At the start of the simulation, the kinetic energy first grew rapidly up to about 90% of this upper bound. Then, floes started to interact and the kinetic

energy decreased due to energy dissipation through frictional contacts and/or collisions (if $\varepsilon < 1$). For the partly jammed configurations (tests 1, 2, and 5), the energy stabilized toward a low value corresponding to the free drift of the unjammed floes.

Figure 22 shows the variations in normal contact impulses for tests 1 and 3. As indicated above, the contact impulse is a contact force multiplied by a time. The signal is highly intermittent, with each peak corresponding to one or more collisions occurring at a given time. In the case of partly jammed configurations, the total impulse stabilizes toward a nearly constant value corresponding to the impulse needed to keep the floes jammed.

4.2. Drift of an Assembly of Floes Under Varying Wind and Current

We consider an assembly of 350 ice floes of various shapes and sizes drifting in an open ocean under spatially constant but varying in time wind and ocean surface current (see Figure 23). Wind forcing has been obtained from a time interpolation of the ERA interim dataset sampled in February 2008 in the Barents sea at $(80.2°\text{N}, 36.8°\text{E})$. This position is close to the ice edge at that time. Surface current has been obtained from the TOPAZ ocean-sea ice model [see *Sakov et al.*, 2012] at the same time and place. The initial configuration is as follows: the floe shapes are randomly chosen within a catalog of shapes extracted from aerial images, whereas the floe sizes $s_f = \sqrt{S/\pi}$ are set to be distributed according to a power law $P(> s_f) \sim s_f^{-\alpha}$, with $\alpha = 1.5$, in agreement with classical observed values [see e.g., *Weiss*, 2003], and with an upper cutoff of 250 m. The individual floe thicknesses are chosen randomly (uniform distribution) between 0.25 and 0.38 m. The ice floes are then assembled

Table 2. Variation of the Parameters Between Tests for Simulation Setup 3.1

Test Number	Friction μ	Restitution ϵ	Coriolis Parameter f
1	0.7	0.35	0
2	0.7	0.6	0
3	0.7	1	0
4	0.5	0.6	0
5	0.7	0.35	$1.44\times10^{-4}\text{s}^{-1}$

Test 1 ($\varepsilon = 0.35$)   2h04   3h40

Test 2 ($\varepsilon = 0.6$)
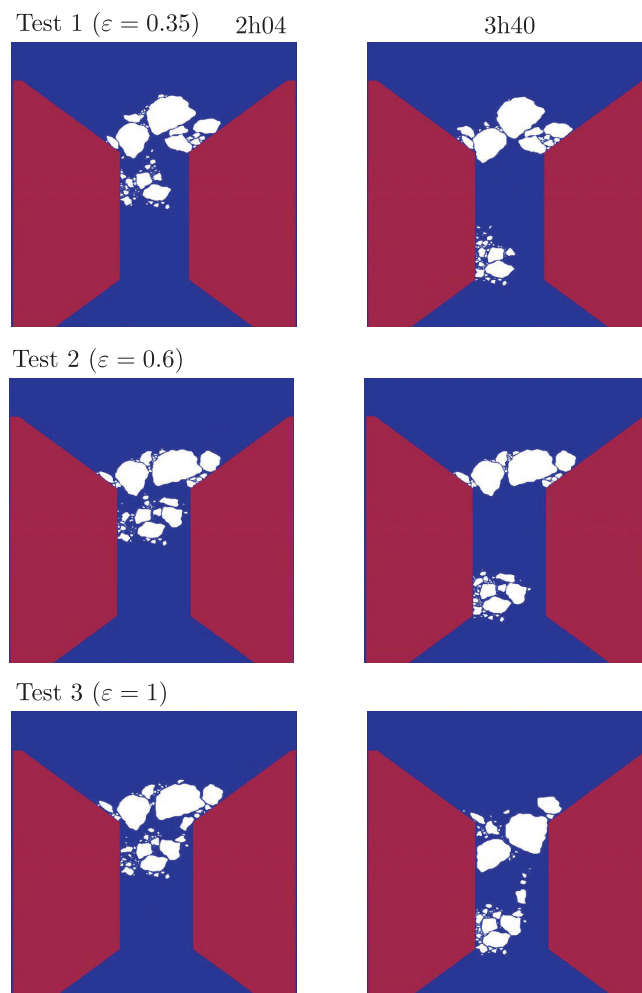
Test 3 ($\varepsilon = 1$)

Figure 17. Simulation 3.1 images (variation of the restitution coefficient ε).

to reach an average sea ice concentration of 60%, typical of the MIZ, over a square of 1.2×1.2 km^2.

Initially, the ice floes are at rest. The trajectories of the ice floes during the week-long simulation are shown in Figure 24. From this large-scale perspective, the ice floes remain grouped together and drift over large distances (km s) in response to the varying wind forcing. On the other hand, at the scale of the assembly, several phenomena are observed:

1. During the first 2 days of simulation, when both wind and current directions are roughly constant, the ice floes disperse and the concentration within the initial square decreases to 45% (see Figures 23 and 25). However, following brutal rotations of the forcing, the ice floes reassemble partially and the concentration rise up again until 54%.

2. During the simulation, the ice floe form progressively groups (or clusters) of floes separated by open water (see Figure 25). This clustering process is well known [*Toyota et al.*, 2011] and has been studied from a molecular dynamics sea model with perfectly circular ice floes [*Herman*, 2011]. It results from the size-dependent equilibrium velocity of the floes [*Herman*, 2011] and from the dissipation of kinetic energy during the collisions.

3. The number of collisions per hours rises during the first 2 days to reach an average value of about 10^5 when clusters of floes are formed (see Figure 23). This simulation possibly suggests different drift and dispersion regimes: a large-scale regime essentially driven by the forcing, and a *collisional* regime at small scales. A thorough statistical analysis of floes trajectories [see *Rampal et al.*, 2008, 2009] obtained from different simulations would be needed to explore this in details.

With this drifting configuration, we tested the sensitivity of our model to the methodology used to deal with the contact points; that is, if we deal with all contact points simultaneously or only the contact points leading to an interpenetration (see section 2.4.2). We simulated the same assembly of 350 floes and with the same atmospheric and oceanic conditions, changing only the manner to deal with the contact points. From the large-scale perspective of Figure 24, the results of the two simulations are nearly indistinguishable. At the scale of individual floes, some differences are perceptible, but the pattern of floes clusters remains similar (see Figure 26).

5. Discussion and Conclusions

The model presented in this paper was built to describe the dynamic behavior of a large number of ice floes of any size and geometry, while keeping within a reasonable processing time. Although our model does not consider the energy dispersion due to vibrational and wave effects, it accurately describes a large range
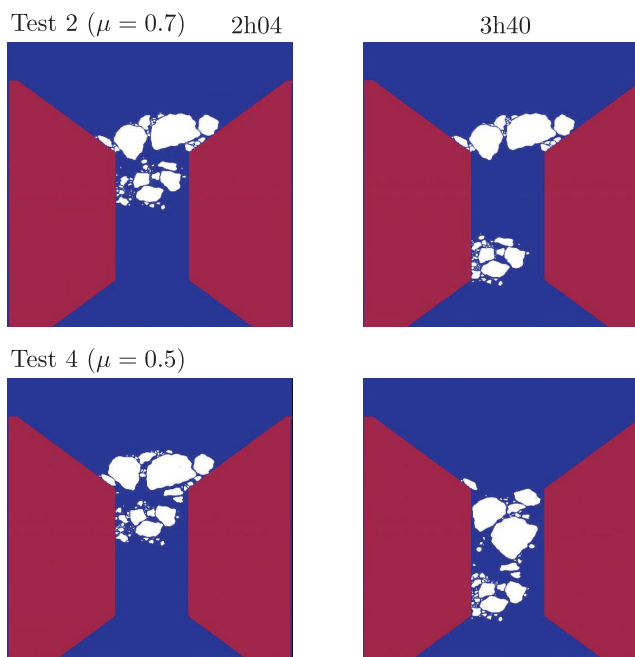
Test 2 ($\mu = 0.7$)   2h04   3h40

Test 4 ($\mu = 0.5$)

Figure 18. Simulation 3.1 images (variation of the friction coefficient μ).

of collisional behaviors (see section 3.1). In addition, the linear and angular momentums as well as the kinetic energy are conserved when elastic collisions are considered.

The next step will be to better estimate the restitution coefficient ε, and to further validate the model either using more realistic experiments performed in ice test basins, or using in situ observations. With in situ observations, the trajectories of ice-tethered buoys drifting within, for example, the marginal ice zone would
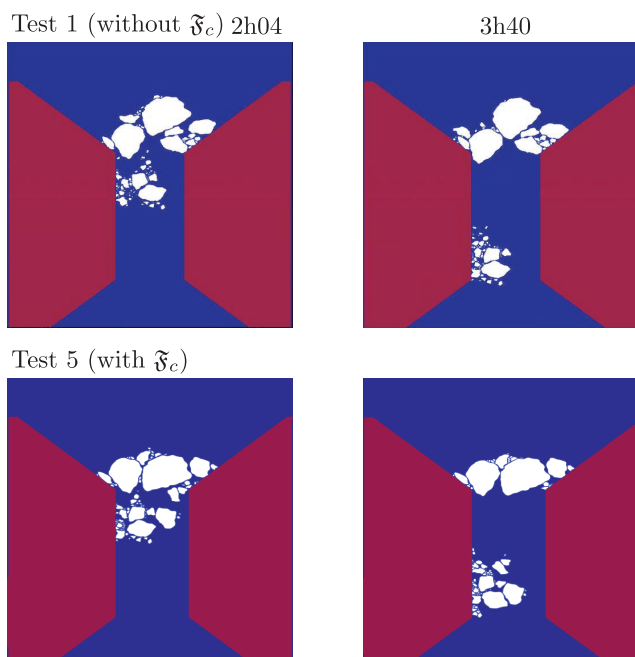
Test 1 (without $\mathfrak{F}_c$) 2h04   3h40

Test 5 (with $\mathfrak{F}_c$)

Figure 19. Simulation 3.1 images (with or without the Coriolis effect $\mathfrak{F}_c$).
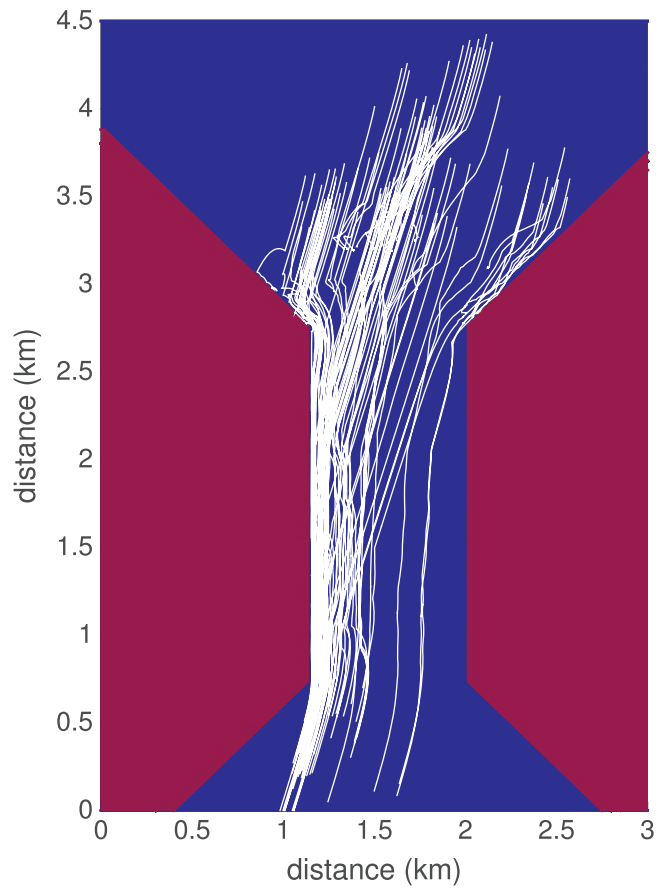
Figure 20. Center of mass trajectories for test 5 of simulation setup 3.1.
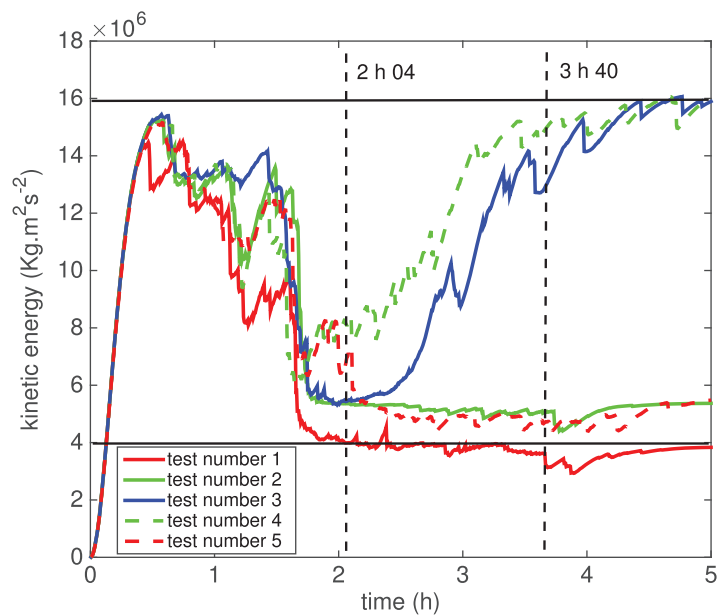

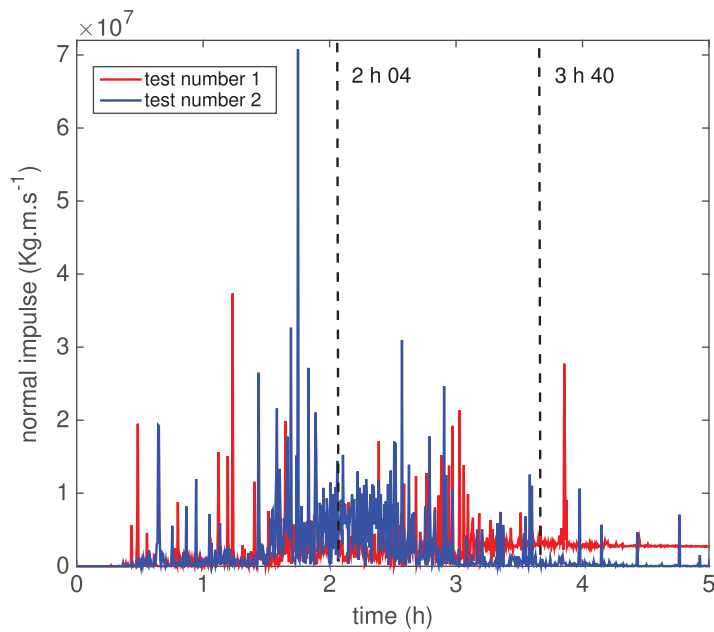**Figure 21.** Variation of the kinetic energy (3.1).

Figure 22. Variation of the normal impulse (3.1).

be an important source of information. However, a direct, deterministic comparison of modeled trajectories with observed trajectories will be difficult, especially because the geometrical characteristics of the floe assembly (size, shape, thickness, and spatial arrangement of the floes) are rarely known. Instead, a
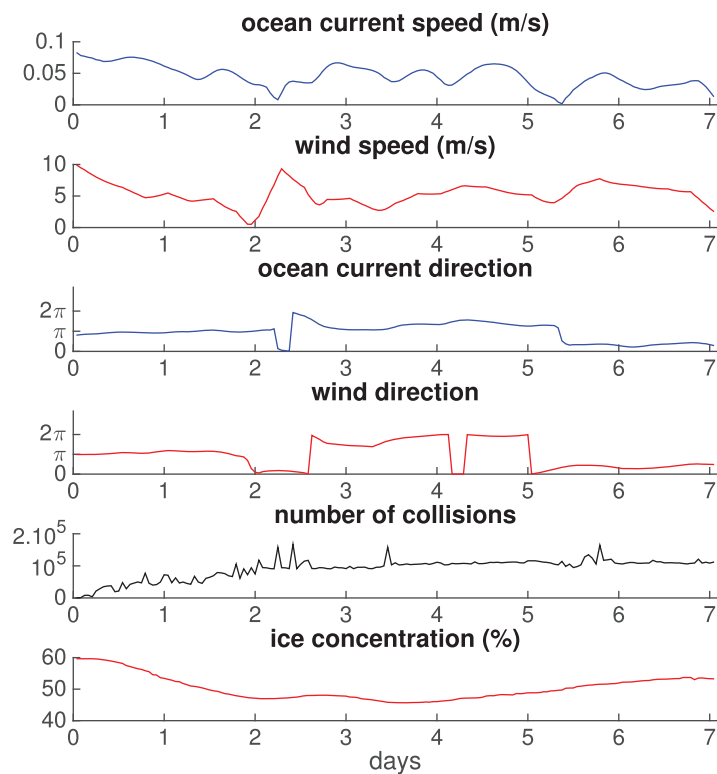

Figure 23. Simulation 3.2: wind and surface current characteristics over the 7 days; number of collisions per hour, and ice concentration.
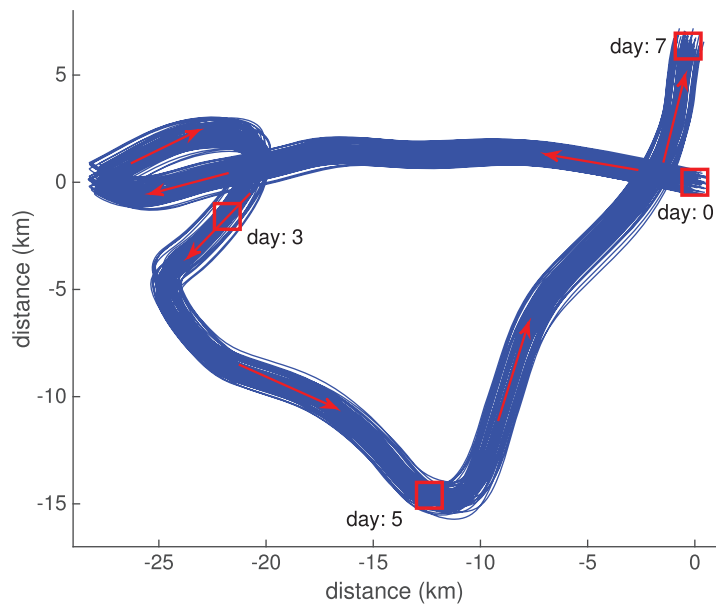
Figure 24. Simulation 3.2: ice floes trajectories during 7 days.

comparison in terms of statistical properties of the velocities [see e.g., *Rampal et al.*, 2009] might be more promising.

As stressed in section 1, in the present version of the model, the main simplifications are the absence of ice rheology and the use of a constant and *universal* coefficient of restitution. To improve this aspect in the future, it will be necessary to combine this model with a rheological as well as a damage model within each ice floe to provide a more physical and detailed description of kinetic energy dissipation during collisions.
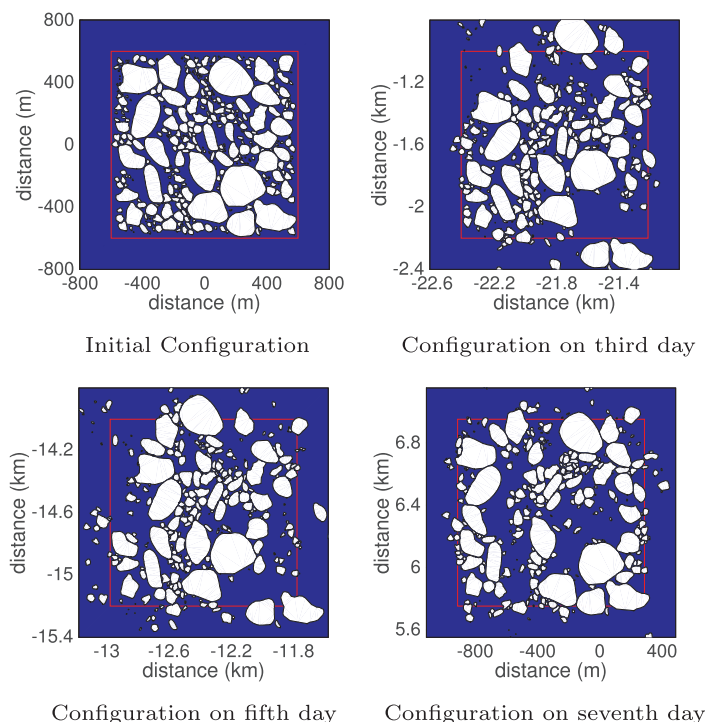

Figure 25. Simulation 3.2: configuration of ice floes at different times.
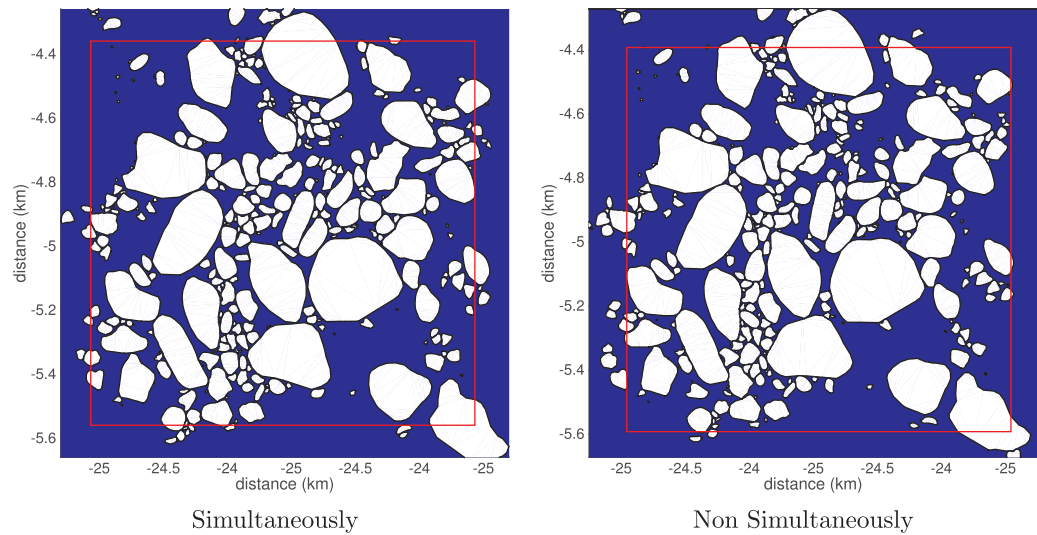
Figure 26. Simulation 3.2: difference between the clusters of floes according to the methodology used to deal with the contact points at 84 h (3.5 days).

The coupling with a simplified ocean model considering an oceanic boundary layer homogeneous over the simulated domain ($\mathbf{u}_w$ spatially constant) will represent another improvement. Finally, in terms of computing optimization, one important direction of research will be the parallel implementation of our model on GPU. To do this, a structure of clusters will be developed. This structure will consist in gathering ice floes interacting with each other into the same cluster. In a cluster, the ice floes will evolve with the same time step and each cluster will follow its own rhythm. Indeed, not all the floe/floe interactions need to be described with the same time step. The main advantage of this approach is that it can deal with each cluster in parallel, thus making it possible to handle a very large number of ice floes within a reasonable computing time.

Notation

$\mathbf{A}^T$	transpose of matrix $\mathbf{A}$.
$\mathbf{d}_{slip}$	sliding direction.
$d(p, \Omega)$	minimum distance between a point p and an ice floe Ω.
$\mathbf{D}$	matrix containing the coordinates of the tangent of the contacts.
$\mathcal{D}^k$	disk of level k.
E	kinetic energy of ice floes.
E^-	kinetic energy of ice floes before collisions.
E^d	kinetic energy of ice floes after a decompression phase.
$\mathfrak{C}$	set of vertices for the mesh border of an ice floe.
$\mathfrak{F}_c$	Coriolis effect.
G	mass center of an ice floe.
h	thickness of an ice floe.
I	moment of inertia of an ice floe.
$\mathcal{I}$	impulse.
$\mathcal{I}_{kj}$	impulse applied to ice floe Ω_k due to a contact at contact point p_j.
$\mathbf{J}$	matrix containing the coordinates of the normal of contacts.
m	number of contact points.
M	mass of an ice floe.
$\mathbf{M}$	matrix containing the mass and the moment of inertia of ice floes.
n	number of ice floes.
$\mathbf{N}$	normal of a contact.

p	contact point.
$\mathcal{P}_i^c$	set of contact points for ice floe Ω_i.
$\mathbf{r}_{ij}$	vector pointing from the mass center of the ice floe Ω_i to a mesh point $j \in \Omega_i$.
$\mathcal{R}$	contact frame.
S	surface of an ice floe.
t	time during the simulation.
t^*	timing of a contact.
t^-	time before a contact.
t^+	time after a contact.
t^c	time after a compression phase.
t^d	time after a decompression phase.
$\mathbf{T}$	tangent of a contact.
$\mathbf{v}_j^R$	relative velocity of contact point p_j.
$\mathbf{V}$	velocity of the mass center of an ice floe.
$\mathbf{W}$	vector of the mass center and angular velocities of ice floes.
$\mathbf{W}_i$	mass center and angular velocities of ice floe Ω_i.
$\tilde{\mathbf{W}}$	linear combination between $\mathbf{W}(t^c)$ and $\mathbf{W}(t^-)$.
$\mathcal{Z}$	collision zone.
α	vector of α_j.
α_j	magnitude of the relative contact velocity $\mathbf{v}_j^R$.
α^c	vector of α_j after a compression phase.
α^d	vector of α_j after a decompression phase.
β	vector of β_j.
β_j	tangential contact impulse of contact point p_j.
β^c	vector of β_j after a compression phase.
β^d	vector of β_j after a decompression phase.
$\tilde{\beta}$	vector of $\tilde{\beta}_j$.
$\tilde{\beta}_j$	vector containing $-\beta_j$ and β_j.
δ	minimum distance between two ice floes.
Δt	time step.
Δt_i	time step associated with ice floe Ω_i.
ΔT	time step for the simulation.
ε	restitution coefficient.
η	threshold distance.
λ	vector of λ_j.
λ_j	normal contact impulse for contact point p_j.
λ^c	vector of λ_j after a compression phase.
λ^d	vector of λ_j after a decompression phase.
μ	friction coefficient.
τ_a	atmospheric skin drag per unit area.
τ_w	oceanic skin drag per unit area.
ω	angular velocity of an ice floe.
Ω	ice floe.

References

Anitescu, M., and F. A. Potra (1997), Formulating dynamic multi-rigid-body contact problems with friction as solvable linear complementarity problems, *Nonlinear Dyn.*, *14*(3), 231–247.

Anitescu, M., F. A. Potra, and D. E. Stewart (1999), Time-stepping for three-dimensional rigid body dynamics, *Comput. Methods Appl. Mech. Eng.*, *177*, 183–197.

Cameron, S. A. (1990), Collision detection by four-dimensional intersection testing, *IEEE Trans. Robotics Autom.*, *6*(3), 291–302.

Cottle, R. W., J.-S. Pang, and R. E. Stone (1992), *The Linear Complementarity Problem*, Siam, Philadelphia.

Delassus, E. (1917), Mémoire sur la théorie des liaisons finies unilatérales, *Ann. Sci. Ecole Normale Super.*, *34*, 95–179.

Drumwright, W., and D. Shell (2011), An evaluation of methods for modeling contact in multibody simulation, *IEEE Trans. Robotics Autom.*, 1695–1701.

Dumont, D., Y. Lévesque, A. Bihan-Poudec, and E. Bismuth (2013), Image processing report, CITEPH 64–2012 project, BGO First, Oceanide, report.

Feltham, D. L. (2008), Sea ice rheology, *Annu. Rev. Fluid Mech.*, *40*, 91–112.

Girard, L., S. Bouillon, J. Weiss, D. Amitrano, T. Fichefet, and V. Legat (2011), A new modeling framework for sea-ice mechanics based on elasto-brittle rheology, *Ann. Glaciol.*, *52*(57), 123–132.

Hadama, K., and Y. Hori (1996), Octree-based approach to real-time collision-free path planning for robot manipulator, in *Proceedings of 1996 4th International Workshop on Advanced Motion Control*, *ACM96-MIE*, vol. 2, pp. 705–710, IEEE.

Hamlin, G. J., R. B. Kelley, and J. Tornero (1992), Efficient distance calculation using the spherically-extended polytope (s-tope) model, *IEEE Trans. Robotics Autom.*, *3*, 2502–2507.

Herman, A. (2011), Molecular-dynamics simulation of clustering processes in sea-ice floes, *Phys. Rev. E*, *84*, 056104.

Herman, A. (2013), Numerical modeling of force and contact networks in fragmented sea ice, *Ann. Glaciol.*, *54*(62), 114–120.

Hopkins, M. A. (1996), On the mesoscale interaction of lead ice and floes, *J. Geophys. Res.*, *101*(C8), 18,315–18,326.

Hopkins, M. A. (1998), Four stages of pressure ridging, *J. Geophys. Res.*, *103*(C10), 21,883–21,891.

Hopkins, M. A., S. Frankenstein, and A. S. Thorndike (2004), Formation of an aggregate scale in arctic sea ice, *J. Geophys. Res.*, *109*, C01032, doi:10.1029/2003JC001855.

Hunkins, K. (1975), Oceanic boundary layer and stress beneath a drifting ice floe, *J. Geophys. Res.*, *80*(24), 3425–3433.

Liu, C., Z. Zhen, and B. Brogliato (2008), Frictionless multiple impacts in multibody systems. I. Theoretical framework, *Proc. R. Soc. A*, *464*, 3193–3211.

McBean, G. (1986), The atmospheric boundary layer, in *The Geophysics of Sea Ice*, pp. 283–338, Springer-Verlag, N. Y.

McNamara, S. (2011), Molecular dynamics method, in *Discrete Numerical Modeling of Granular Materials*, pp. 1–25, Wiley-ISTE, N. Y.

McPhee, M. (1986), The upper ocean, in *The Geophysics of Sea Ice*, pp. 339–395, Springer-Verlag, N. Y.

Metrikin, I., S. Løset, N. A. Jenssen, and S. Kerkeni (2013), Numerical simulation of dynamic positioning in ice, *Mar. Technol. Soc. J.*, *47*(2), 14–30.

Moreau, J. J. (1963), Les liaisons unilatérales et le principe de gauss, *C. R. Hebd. Seances Acad. Sci.*, *256*, 871–874.

Nansen, F. (1902), Oceanography of the north polar basin: The Norwegian north polar expedition 1893–96, *Sci. Results*, *3*(9), 427.

Nguyen, N. S., and B. Brogliato (2014), *Multiple Impacts in Dissipative Granular Chains*, vol. 72, Springer, Berlin Heidelberg.

Paavilainen, J., J. Tuhkuri, and A. Polojarvi (2011), 2d numerical simulations of ice rubble formation process against an inclined structure, *Cold Reg. Sci. Technol.*, *68*(1–2), 20–34.

Pfeiffer, F., and C. Glocker (1996), *Multibody Dynamics With Unilateral Contacts*, John Wiley and Sons, N. Y.

Quinlan, S. (1994), Efficient distance computation between non-convex object, *IEEE Trans. Robotics Autom.*, *4*, 3324–3329.

Rampal, P., J. Weiss, D. Marsan, R. Lindsay, and H. Stern (2008), Scaling properties of sea ice deformation from buoy dispersion analysis, *J. Geophys. Res.*, *113*, C03002, doi:10.1029/2007JC004143.

Rampal, P., J. Weiss, D. Marsan, and M. Bourgoin (2009), Arctic sea ice velocity field: General circulation and turbulent-like fluctuations, *J. Geophys. Res.*, *114*, C10014, doi:10.1029/2008JC005227.

Rathod, H. T., K. V. Nagaraja, B. Venkatesudu, and N. Ramesh (2004), Gauss Legendre quadrature over a triangle, *Short Commun. Indian Inst. Sci.*, *84*, 188–193.

Sakov, P., F. Counillon, L. Bertino, K. A. Lisæter, P. R. Oke, and A. Korablev (2012), Topaz4: An ocean-sea ice data assimilation system for the north Atlantic and Arctic, *Ocean Sci.*, *8*(4), 633–656.

Signorini, A. (1933), *Sopra Alcune Questioni di Elastostatica*, Atti Soc. Ital. per il Prog. delle Sci., Roma.

Smith, B., D. M. Kaufman, E. Vouga, R. Tamstorf, and E. Grinspun (2012), Reflections on simultaneous impact, *ACM Trans. Graph.*, *31*(4), 106: 1–106:12.

Stewart, D. (2000), Rigid-body dynamics with friction and impact, *SIAM Rev.*, *42*, 3–39.

Stewart, D., and J. Trinkle (1996), An implicit time-stepping scheme for rigid body dynamics with inelastic collisions and coulomb friction, *Int. J. Numer. Methods Eng.*, *39*, 2673–2691.

Stroeve, J. C., V. Kattsov, A. P. Barrett, M. C. Serreze, T. Pavlova, M. M. Holland, and W. N. Meier (2012b), Trends in arctic sea ice extent from CMIP5, CMIP3 and observations, *Geophys. Res. Lett.*, *39*, L16502, doi:10.1029/2012GL052676.

Toyota, T., C. Haas, and T. Tamura (2011), Size distribution and shape properties of relatively small sea-ice floes in the Antarctic marginal ice zone in late winter, *Deep Sea Res., Part II*, *58*(9–10), 1182–1193.

Tsai, V. C., and D. E. McNamara (2011), Quantifying the influence of sea ice on ocean microseism using observations from the bering sea, Alaska, *Geophys. Res. Lett.*, *38*, L22502, doi:10.1029/2011GL049791.

Wang, J., and A. Derradji-Aouat (2010), *Ship Performance in Broken Ice Floes—Preliminary Numerical Simulations*, Inst. for Ocean Technol., Natl. Res. Counc., St. John's, NL.

Weiss, J. (2003), Scaling of fracture and faulting in ice on earth, *Surv. Geophys.*, *24*, 185–227.

Weiss, J. (2013), *Drift, Deformation and Fracture of Sea Ice—A Perspective Across Scales*, Springer, Netherlands.

Wilchinsky, A. V., D. L. Feltham, and M. A. Hopkins (2010), Effect of shear rupture on aggregate scale formation in sea ice, *J. Geophys. Res.*, *115*, C10002, doi:10.1029/2009JC006043.